Research Article

Designing a thermodynamically stable and intrinsically ductile refractory alloy

Sufyan M. Shaikh [a], B.S. Murty [a,b], Satyesh K. Yadav [a,c,*]

[a] Department of Metallurgical and Materials Engineering, Indian Institute of Technology Madras, Chennai 600036, Tamil Nadu, India
[b] Materials Science & Metallurgical Engineering, Indian Institute of Technology Hyderabad, Kandi 502285, Telangana, India
[c] Center for Atomistic Modeling and Materials Design, Indian Institute of Technology Madras, Chennai 600036, Tamil Nadu, India

ARTICLE INFO

ABSTRACT

Developing ductile refractory alloys have remained a challenge. Decreasing the valence electron concentration of refractory alloys has been widely suggested for improving their ductility. However, Re has been used to ductilize W, which goes against the low valency suggestion. The thermodynamic stability of refractory alloys has never been considered while suggesting alloying elements to improve ductility. Here we use first-principles density functional theory simulations to unravel the role of enthalpy of formation in improving the intrinsic ductility of refractory alloys. The intrinsic ductility is assessed using the D-parameter, which is the ratio of surface energy and unstable stacking fault energy. We studied 25 equiatomic binary refractory alloys and found that positive enthalpy of formation improves ductility. The small positive enthalpy of formation could be compensated by sufficiently large entropy; hence the alloy is expected to be a single phase. Our present work explains the role of high-valency and low-valency alloying elements in improving the ductility of refractory alloys. These findings provide a path to design thermodynamically stable and intrinsically ductile high-temperature alloys.

1. Introduction

The continued cost pressures and ever stringent environmental norms have pushed aerospace and power generation industries to improve the overall efficiency of their jet-engines and gas-turbines [1]. Higher operating temperatures would lead to better thermodynamic efficiency in these propulsion and energy conversion systems [2,3]. The Ni-based superalloys have ruled this application domain for the past more than six decades [4]. The melting point of the base metal Ni (T_m=1455℃) limits the highest operating temperature of these Ni-based superalloys [1,5]. Alloys based on refractory metals show great potential in this domain due to their high melting-points and their ability to maintain mechanical properties at temperatures higher than the current Ni-based superalloys [5]. Refractory alloys are based on Group IV, V, and VI metals [6–8]. These elements have very high melting-points ($T_m > > 1800℃$) and predominantly BCC crystal structure which limits their ductility at ambient temperatures.

The lack of deformability at lower temperatures makes refractory alloys difficult to manufacture, which creates a bottleneck in developing them for various applications. Mo has been ductilized by adding 25 at% of Ti/Zr/Hf, indicating that HCP alloying additions should ductilize Mo [9]. W has been ductilized by Re addition [10,11], which has been explained through simulations as reduction in the overall ustable stacking fault energy (γ_{usfe}) of the alloy [12]. There have been conflicting suggestions about alloying additions to make W deformable [12,13]. Qian et al. [13] suggest Re addition to W leads to decreased generalized stacking fault energy (γ_{gsfe}) and increased ductility, whereas Ta addition has the opposite effect. However, in Qian's work, the chemistry of the supercell was $W_{47}X$ (X = Ta or Re), which may not be an accurate representation of a concentrated alloy. Re addition in 12.5 at% or 25 at% to W has been shown to decrease the shear resistance of {110} < 111 > and {112} < 111 > slip system, which in turn improves the ductility of W [14]. Reducing the valence electron concentration (VEC) [15] and reducing the lattice distortion in Nb-based alloys has been shown to decrease the Peierls stress [16] which in turn makes alloy deformable. The addition of Ti has been shown to ductilize NbMoTaW and NbZrTa alloys [17,18]. Decreasing Ta has been shown to decrease the resolved shear stress of the TiZrHfTa, enhancing its ductility [19]. Sheikh et al. [20] suggest alloying with Ti, Zr, and Hf (HCP elements) should ductilize the

* Corresponding author.
E-mail address: satyesh@iitm.ac.in (S.K. Yadav).

Table 1

Ductilizing strategies reported in literature for refractory metals and alloys. (M- Modeling, E-Experiments).

Metal/Alloy	Ductilizing strategy	Method	Reference
W	Increase Ta (↓VEC), Add Re (↑ VEC)	M	[12]
W	Increase Re (↑ VEC)	E,M	[14,21]
W	Add Re (↑ VEC)	E	[11]
Mo	Add Ti, Zr, Hf (↓ VEC)	M	[9]
Mo	Add low valency elements (↓ VEC)	M	[22]
Nb	Add low valency elements (↓ VEC)	M	[15,16]
TiZrHfTa	Decrease Ta (↓ VEC)	M	[19]
NbZrTaTi	Decrease Ta (↓ VEC), Increase Ti (↓ VEC)	E,M	[18]
NbMoTaW	Add Ti (↓ VEC)	E	[17]

refractory alloys as it reduces the VEC; this goes against the high valency Re addition to ductilize W. The suggestions given in literature on ductilizing refractory metals and alloys are summarized in Table 1.

From the Table 1, we observed a common strategy to ductilize refractory metals and alloys is by decreasing their VEC. However, Re addition to ductilize W remains an exception to the low VEC suggestion. We found that the focus in earlier studies has been on improving the ductility of these alloys without considering their thermodynamic stability. The strength and ductility of FCC alloys can be regulated by modifying the stacking fault energy (γ_{sfe}), tuning short-range order, and lattice distortion, as reported in [23–26–29,30,31]. Large decrease in γ_{sfe} of FCC alloys (as compared to their composition averaged γ_{sfe}) due to alloying has already been observed in Co-Cr-Fe-Mn-Ni alloy and its sub-systems [32–35–38,39].

We conclude from various reports on ductilizing refractory alloys that HCP metals such as Ti, Zr, Hf which have low γ_{sfe}, are added to reduce the overall γ_{usfe} of the alloy; which suggests that the Rule-of-Mixtures (ROM) dictates the overall γ_{usfe} of the alloy. Most of the earlier studies selected alloying elements to get maximum decrease in the overall γ_{usfe} or increase in the intrinsic ductility of the alloy, without considering its thermodynamic stability. This calls for a comprehensive study on the role of various alloying elements on the deformability and thermodynamic stability of refractory alloys. The stacking fault energy (γ_{sfe}) of NiFe [38,39] and CoCrFeNi [32,34] calculated using first-principles density functional theory (DFT) simulations matches with their respective experimental value. This shows that the γ_{sfe} can be accurately predicted using DFT. Present work addresses these issues using DFT simulations as atomistic modeling based on DFT provides an accurate description of configurational and chemical space. Our present work gives a fundamental explanation of the role of both high valency as well as low valency elements in ductilizing W and other refractory metals and alloys.

2. Methods

Ti, Zr, Hf, V, Nb, Ta, Mo, W, Re, and their 30 equiatomic binary alloy systems (excluding alloys made up of only HCP elements) are studied using DFT simulations. Lattice parameter (a, c, Å), enthalpy of formation (ΔE_f, eV/Atom), unstable stacking fault energy (USFE, γ_{usfe}, mJ/m^2), and surface energy (γ_s, mJ/m^2) are calculated for V, Nb, Ta, Mo, W, and 30 equiatomic binary alloys in BCC symmetry. For Ti, Zr, Hf, and Re, γ_{usfe} is calculated for {0001}<11$\bar{2}$0> slip system, γ_s is calculated for {0001} plane, a, c, and ΔE_f are calculated for HCP crystal structure.

2.1. Special quasirandom structures, supercell

Special quasirandom structures (SQS) are used to capture chemical disorder in the alloys. SQS are generated using MCSQS code from Alloy Theoretic Automatic Toolkit (ATAT) [40,41] with pair, triplet, and quadruplet correlations with cut-off distance equal to the BCC unit cell lattice parameter (second nearest neighbor distance). The ΔE_f and lattice parameter are calculated with 128 atoms SQS generated using a BCC unit cell repeated four times each in < 100 > directions. The experimental values of lattice parameters are taken from Ref.[42]. The reported lattice parameters were within 1 % deviation of their experimental values. The supercells were visualized using VESTA software [43].

2.2. First-principles calculations

The DFT calculations were performed using Vienna Ab-initio Simulation Package (VASP) with plane-wave basis and projector augmented wave (PAW) pseudopotentials [44–46]. For all calculations, a plane wave kinetic energy cutoff of at least 1.3 times the maximum given in the pseudopotential file was used. The electronic exchange-correlation effects were calculated by Perdew-Burke-Erzernhoff generalized gradient approximation (PBE-GGA) [47,48]. Methfessel-Paxton smearing method with 0.2 eV width was used [49]. Structural relaxation was terminated when the forces on atoms become less than 1 meV/Å. Tetrahedron method with Blöch correction was used for energy calculation [45]. The Brillouin zone sampling was performed using Monkhorst-Pack [50] scheme with automatically generated mesh with k-point spacing of less than $2\pi \times 0.03$ Å^{-1}.

3. Results and discussions

To better understand the factors affecting the intrinsic ductility of concentrated BCC alloys, refractory equiatomic binary alloys made from Group-IV (Ti, Zr, Hf), Group-V(V, Nb, Ta), Group-VI(Mo, W), and Group-VII(Re) elements are studied. The γ_{usfe} calculation of solid solutions using DFT, is bound to have errors due to the change in local chemistry while the interface is being sheared and due to the stoichiometry of the shearing interface. The magnitude of this error could alter conclusions, hence an estimate of this error is important while making comparisons across alloys. Here we have estimated the maximum error that gets introduced, and discuss ways to minimize it, making our conclusions reliable.

To address these shortcomings which we found in the literature, a DFT-based workflow is developed to calculate a,c, ΔE_f, γ_{usfe}, and surface energy (γ_s) (Fig. 1). The workflow is elaborated further in the subsequent sections. The results are shown in the form of heat maps in Fig. 2. Additional information can be found in the supplementary file.

3.1. Enthalpy of formation (ΔE_f)

The stability of an alloy (solid solution) is dictated by the Gibbs energy of its constituent phases as,

$$\Delta G = \Delta H - T\Delta S$$
$$= \Delta E_f + \Delta(PV) - T\{\Delta S_{config} + \Delta S_{vib} + \Delta S_{mag} + \Delta S_{elec}\}$$

where ΔE_f is the enthalpy of formation at 0 K, $\Delta(PV)$ is the pressure-volume term, ΔS_{config} is the configurational entropy, ΔS_{vib} is the vibrational entropy, ΔS_{mag} is the magnetic entropy, ΔS_{elec} is the electronic entropy. The $\Delta(PV)$ term can be ignored [51]. Therefore the equation becomes,

$$\Delta G = \Delta E_f - T\Delta S_{config} - T\{\Delta S_{vib} + \Delta S_{mag} + \Delta S_{elec}\}$$

For an equiatomic binary alloy AB, ΔE_f is calculated with the relation [52],
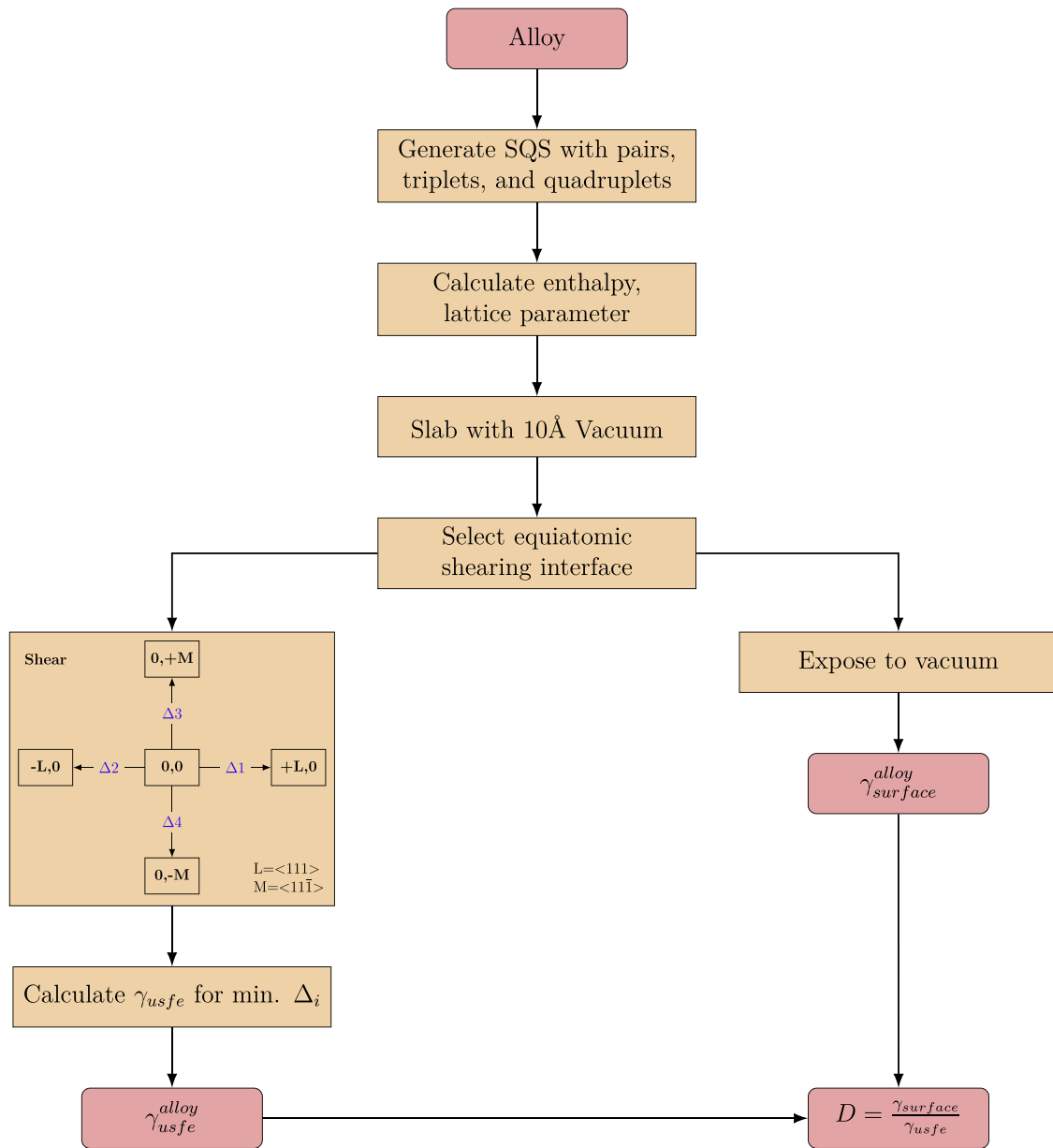
$$\Delta E_f^{AB} = E_{AB} - 0.5^*(E_A + E_B)$$

Fig. 1. Workflow.

where E_{AB} is the energy per atom of alloy AB in BCC symmetry, E_A and E_B, are the energy of constituents A and B in their most stable phase. All values are in the units of eV/Atom. The 9 alloying elements form a total of 36 equiatomic binary alloys. Out of these 36 alloys, 6 systems containing both the constituents being in HCP crystal structure, are not considered in the present study. Fig. 2a shows the enthalpy of formation (ΔE_f, eV/Atom) values in the form of heat map. We have not considered VRe [53], TaRe [54], HfW [55], ZrW [56], VHf [57], VZr [58], having ΔE_f, − 0.2456, − 0.1942, 0.1114, 0.1477, 0.1631, 0.1710 meV/Atom respectively, for subsequent analysis as they can either form intermetallic (VRe, TaRe) due to very negative ΔE_f or they can segregate (HfW, ZrW, VHf, VZr) due to highly positive ΔE_f. The ΔE_f of alloys considered in present study ranges from − 0.1232 eV/Atom (TaMo) to 0.0994 eV/Atom (WRe).

The ΔE_f value of 0.0994 meV/Atom appear very large for a solid solution to be stable. For an equiatomic binary alloy, the $T\Delta S_{config}$ term has value of about 18 meV/Atom at 300 K. Since WRe forms a stable solid solution [59], we expect that the other entropic contributions would be sufficiently large ($\approx$ 80 meV/Atom) to overcome

the 0.0994 eV/Atom ΔE_f value. Although we take WRe as an extreme case of having the most positive ΔE_f (among the presently considered alloys), depending upon the $T\Delta S_{config}$ and $T\Delta S_{vib}$ values, not all alloys may be stable.

3.2. Unstable stacking-fault energy (γ_{usfe})

Within DFT, the γ_{usfe} is calculated using the relation given below,

$$\gamma_{usfe} = \frac{E_{faulted} - E_{pristine}}{(Area\,of\,Plane)}$$

where the $E_{faulted}$ is the energy of supercell having a stacking fault and the $E_{pristine}$ is the energy of pristine supercell. The {110} < 111 > slip system of BCC metals/alloys has the lowest energy barrier for activation. Therefore, we have chosen the same slip system in present study.
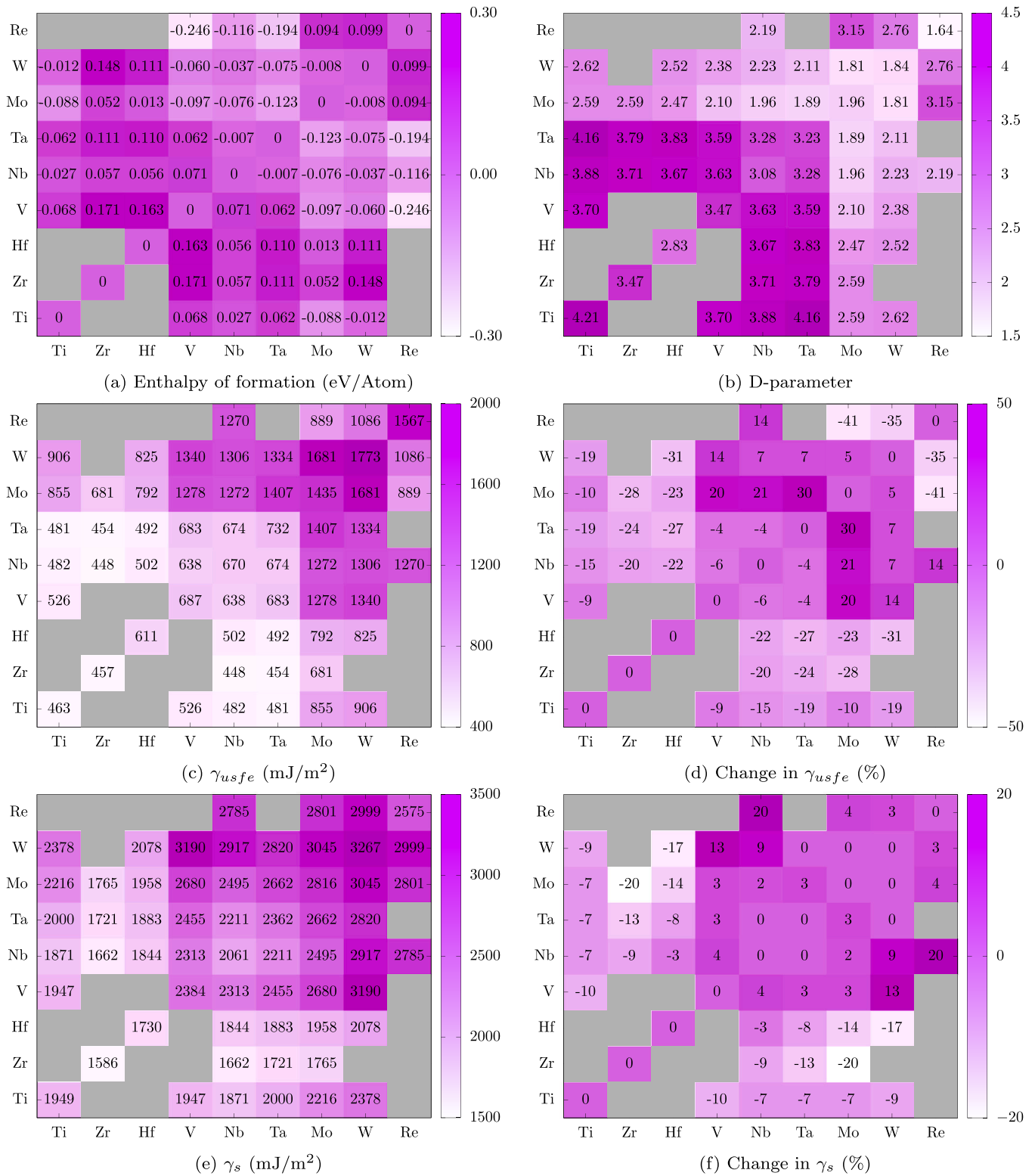
(a) Enthalpy of formation (eV/Atom)

(b) D-parameter

(c) γ_{usfe} (mJ/m^2)

(d) Change in γ_{usfe} (%)

(e) γ_s (mJ/m^2)

(f) Change in γ_s (%)

Fig. 2. Heat maps. Alloys containing both HCP constituents are not considered.

3.2.1. Slip system

The γ_{usfe} of an alloy strongly depends on the γ_{usfe} of its constituent pure metals. In order to understand how the γ_{usfe} of pure elements affect the γ_{usfe} of an alloy, comparison of similar slip systems should be made. Since some of the pure metal constituents of alloy have HCP crystal structure, the {110} < 111 > slip system of BCC should be compared with an equivalent slip system in HCP crystal structure.

The {0001} slip plane in HCP crystal structure have similar close-packed arrangement of atoms as that in {110} slip plane of BCC crystal structure. The {0001} slip plane γ_{sfe} curves of Zr are shown in Fig. 3a for < 11$\bar{2}$0 > and in Fig. 3c for < 10$\bar{1}$0 > slip direction. Fig. 3e shows the γ_{sfe} curve of Nb for {110} < 111 > slip system. From Fig. 3b and f, it is observed that the atomic arrangements in BCC-{110} and HCP-{0001} slip planes is similar. Therefore, from Fig. 3 it is clear
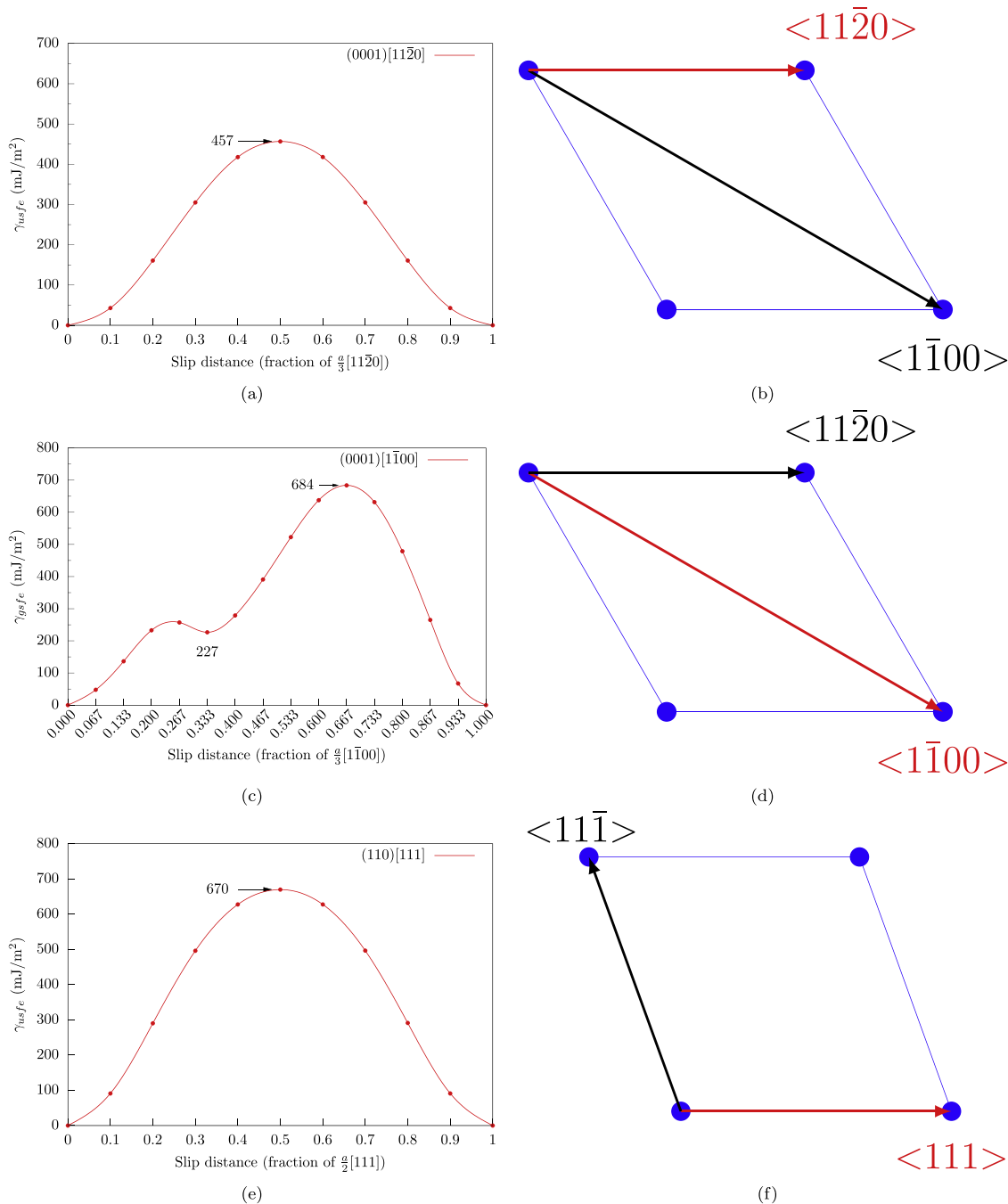
Fig. 3. BCC and HCP slip system comparison. (a)Zr (0001)[11$\bar{2}$0] slip curve, (b)HCP (0001)[11$\bar{2}$0] slip system projection along [0001] direction, (c)Zr (0001)[1$\bar{1}$00] slip curve, (d) HCP (0001)[1$\bar{1}$00] slip system projection along [0001] direction, (e)Nb (110)[111] slip curve, (f)BCC (110)[111] slip system projection along [110] direction. (Out of plane atoms are not shown).

that the {110}< 111 > γ_{usfe} of BCC crystal structure should be compared with the {0001}< 11$\bar{2}$0 > γ_{usfe} of HCP crystal structure.

3.2.2. Shearing interface stoichiometry

Special quasirandom structures (SQS) have been extensively used to predict the γ_{sfe} of alloys due to their simplicity in capturing the inherent chemical disorder present in the alloys [60]. In present work, the SQS supercell with in-plane dimensions equal to 4 and 3 times of the first nearest neighbor distance of the BCC crystal structure are generated (Fig. S1), considering the pair, triplet, and quadruplet correlations with cut-off distance equal to the regular BCC unit cell lattice parameter (second nearest neighbor distance). The supercell had 10 planes of (110)-type giving 9 shearing

interfaces as shown in Fig. S1. A vacuum of 10Å is added to the supercell to prevent interactions due to the periodic boundary condition. To calculate the γ_{usfe}, the atoms in top two planes and bottom two planes were fixed in all directions, whereas, the remaining atoms from the middle six planes were fixed only in slip direction. There are four [111]-type slip directions available for every shearing interface, giving 4 different γ_{usfe} values. Therefore, the same supercell can gives 36 different γ_{usfe} values.

Using the above methodology, we calculated the γ_{usfe} for (110) [111] slip system of WRe alloy (Fig. 4). For any shearing interface the energy change in the pristine and slipped supercell is due to the change in the local bonding environment. Out of the 4 possible γ_{usfe}, we choose the one with the minimum difference in energy of
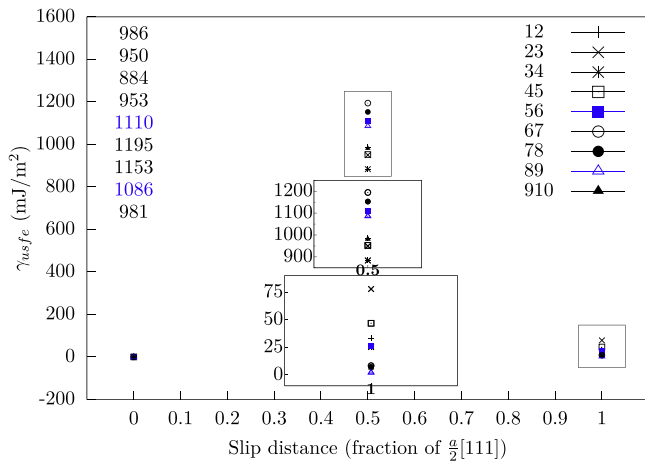
Fig. 4. Comparision between γ_{usfe} values calculated for various shearing interfaces from same supercell of WRe. Legend on the right shows the shearing interface (12 indicates that the shearing interface was between first and second plane). Numbers on left shows the γ_{usfe} value. Upper inset shows the range of γ_{usfe}. Lower inset shows the energy difference between before and after one complete slip by $\bar{b} = \frac{a}{2}[111]$. Blue numbers show the γ_{usfe} of equiatomic shearing interfaces.

pristine and sheared slab as shown in Figs. S2 and S3. Therefore there are 9 γ_{usfe} values shown in in Fig. 4 instead of 36. As observed from Fig. 4, the γ_{usfe} varies from 906 to 1199 mJ/m^2. Similarly the energy difference between pristine and sheared supercell varies from 0.5 to 109 mJ/m^2 (lower inset in Fig. 4). There are two shearing interfaces in Fig. 4 having the same stoichiometry as that of the overall supercell chemistry (equiatomic WRe). These two shearing interfaces give 1110 mJ/m^2 and 1086 mJ/m^2 γ_{usfe} value. It indicates that the 2nd nearest neighbor also influences the γ_{usfe}. We have taken 1086 mJ/m^2 as the γ_{usfe} value of WRe in present study as this shearing interface was having the lowest energy difference of 1.9 mJ/m^2 between the pristine and sheared supercell.

Based on the above discussion, one should consider only the equiatomic shearing interface to calculate the γ_{usfe} of equiatomic alloys. Since the supercell has shearing interfaces that do not have equiatomic stoichiometry, it is assumed that all possible values of γ_{usfe} can exist. The strategy in the literature have been to report an average γ_{usfe} obtained from all shearing interfaces. Such an approach does not assure a specific value of error that gets introduced. From WRe results (Fig. 4), it is clear that stoichiometry strongly affects the γ_{usfe}. That is because of nearest neighbor bond in the shearing interface. Since the intent is to calculate the γ_{usfe} for an equiatomic alloy, we choose the value corresponding to equiatomic shearing

interface. Among the two interfaces that have same stoichiometry in Fig. 4, there is a difference in γ_{usfe} value due to different set of second nearest neighbors. For the rest of the alloys, the obvious choice of γ_{usfe} will be from the shearing interface having the same stoichiometry as that of the supercell. We found that the maximum energy difference between the pristine and the sheared supercell is 60 mJ/ m^2. This error is alloy dependent, whereas the lowest error is 0 mJ/ m^2 in NbTa. Such error estimation which could affect the interpretation has not been discussed in the literature.

3.2.3. On the origin of γ_{usfe} of binary alloys

. Fig. 2c shows the γ_{usfe} calculated using DFT method, in the form of heat map for pure elements and the alloys under study. The HCP elements have the lowest γ_{usfe} except Re. Among the studied pure metals, the overall trend is of increasing γ_{usfe} as we go right in the periodic table from Group-IV to Group-VII. W (1773 mJ/m^3) has the highest γ_{usfe} whereas Zr (457 mJ/m^3) has the lowest γ_{usfe}. For alloys, the γ_{usfe} ranges from 454 mJ/m^2 (TaZr) to 1681 mJ/m^2 (MoW). Fig. 2d shows the change in γ_{usfe} of the alloys from their composition averaged value ($\Delta\gamma_{usfe}$) as calculated below,

$$\Delta\gamma_{usfe} = \frac{\gamma_{usfe}^{DFT} - \gamma_{usfe}^{ROM}}{\gamma_{usfe}^{ROM}} \times 100$$

where the γ_{usfe}^{DFT} is the DFT calculated value and γ_{usfe}^{ROM} is the composition averaged value. The $\Delta\gamma_{usfe}$ ranges from − 41 % (MoRe) to + 20 % (MoV). As observed from Fig. 2c and Fig. 2d, the rule-of-mixtures (ROM) overestimates the γ_{usfe} for a number of alloys. For example, the DFT-calculated γ_{usfe} for WRe and MoRe is 1110 mJ/m^2 and 889 mJ/ m^2 respectively. However the − 35 % (WRe) and − 41 % (MoRe) $\Delta\gamma_{usfe}$ indicates that ROM overestimates the γ_{usfe} by a large margin and is not a reliable method to get the correct values. This also suggests that the γ_{usfe} of alloys is dictated by the nature of bonds between the constituent atoms.

The positive and negative $\Delta\gamma_{usfe}$ can be due to the repulsive or attractive interaction between the constituent atoms. One of the parameter to assess the nature of interaction is enthalpy of formation (ΔE_f). The ΔE_f of equiatomic alloy captures the attractive (negative ΔE_f) or repulsive (positive ΔE_f) interaction between atoms even if the crystal structure of metals that form the alloy are not the same. For example, W and Re have BCC and HCP crystal structure in their pure state, respectively. The ΔE_f of W25-Re75 alloy in BCC crystal structure will have contribution from change in crystal structure of Re from HCP to BCC, apart from the interaction between atoms. In non-equiatomic alloys with different crystal structure of constituents, the ΔE_f does not reflect attractive or repulsive interaction alone, but for alloy with constituent metals in the same
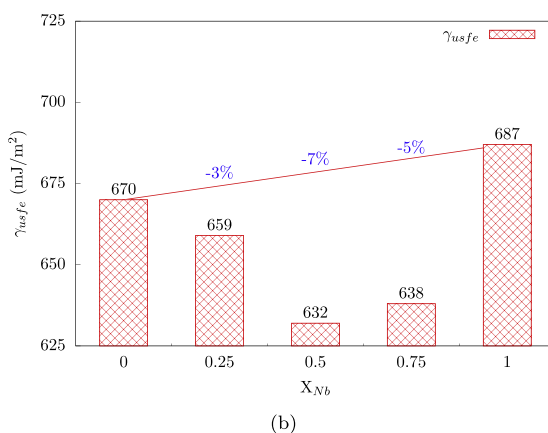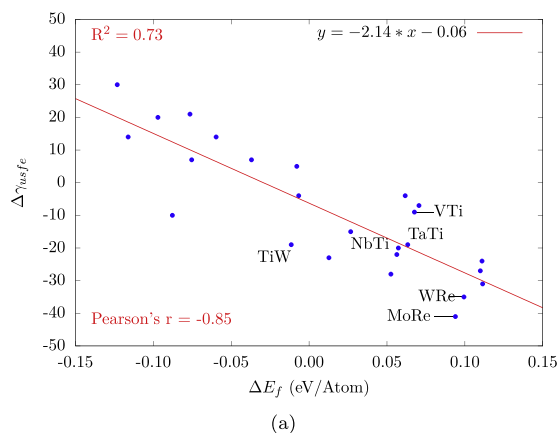

Fig. 5. (a)Change in γ_{usfe} as compared to the composition averaged value vs ΔE_f. (b)(110)[111] γ_{usfe} of Nb-V alloys. Numbers in blue show the change in γ_{usfe} from the composition averaged value.
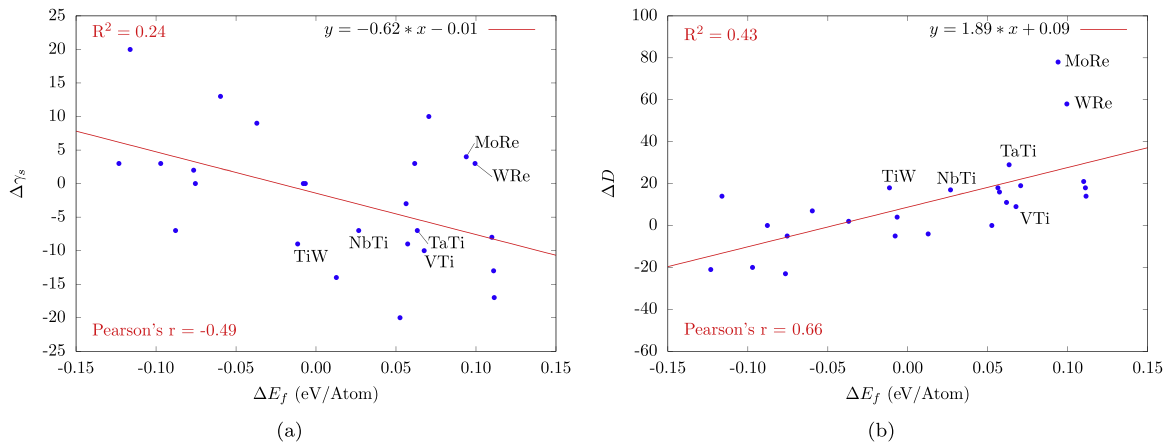
Fig. 6. (a)Change in γ_s as compared to the composition averaged value vs ΔE_f. Enthalpy of formation does not affect the γ_s of alloys. (b)Change in intrinsic ductility (D) as compared to the composition averaged value vs ΔE_f. Positive ΔE_f helps improving the deformability of refractory binary alloys.

crystal structure, ΔE_f of any alloy chemistry will reflect the nature of interaction. Fig. 5a shows the $\Delta\gamma_{usfe}$ vs. ΔE_f. A linear fit to the data in Fig. 5a has a slope of -2.14 with Pearson's r (correlation parameter) of -0.85. This indicates a strong inverse correlation between ΔE_f with $\Delta\gamma_{usfe}$. The ΔE_f is maximum at equiatomic composition as the number of A-B bonds in an AB alloy would be the highest at equiatomic composition. Inverse correlation between $\Delta\gamma_{usfe}$ and ΔE_f suggests that maximum $\Delta\gamma_{usfe}$ (positive or negative) would occur at equiatomic composition. Fig. 5b shows the γ_{usfe} values for $Nb_xV_{(1-x)}$ $\forall$ x $\in$ [0,0.25,0.75,1]. The largest $\Delta\gamma_{usfe}$ occurs at equiatomic concentration (Fig. 5b). The present analysis shows many possible alloy combinations which can lead to reduced γ_{usfe} in refractory binary alloys from their average values. Some of them are highlighted in Fig. 5a.

3.3. Surface energy (γ_s)

Similar to γ_{usfe} calculation, the γ_s is calculated for the interface having equiatomic stoichiometry/formula composition. The equiatomic shearing interface of the supercell is exposed to vacuum of 10Å. The γ_s is calculated using the relation given below,

$$\gamma_s = \frac{E_{with-vacuum} - E_{no-vacuum}}{2 \times (Area of Plane)}$$

where the $E_{with-vacuum}$ is the energy per atom of the supercell with vacuum and $E_{no-vacuum}$ is the energy per atom of the supercell without vacuum. Fig. 2e shows the (110) γ_s calculated using DFT method, in the form of heat map for pure elements and the alloys under study. For Ti, Zr, Hf, and Re, the γ_s is reported for (0001) plane. The γ_s ranges from 3190 mJ/m^2 (VW) to 1662 mJ/m^2 (NbZr). Fig. 2f shows the percentage change in γ_s values of the alloys from their composition averaged values ($\Delta\gamma_s$, calculated similar to $\Delta\gamma_{usfe}$). The $\Delta\gamma_s$ ranges from -20 % (MoZr) to 20 % (NbRe). Fig. 6a shows the $\Delta\gamma_s$ vs. ΔE_f. A linear fit to the data in Fig. 6b has a slope of -0.62 with Pearson's r (correlation parameter) of -0.49. This indicates that the ΔE_f does not strongly influences the γ_s.

3.4. Ductility parameter (D)

The intrinsic ductility parameter (D) quantifies competition between the energy cost of creating a new crack surface and the energy cost of moving a dislocation in the stress field of the crack tip as explained in [61]. The D is defined as the ratio of γ_s to γ_{usfe} [61,62].

$$D = \frac{\gamma_s}{\gamma_{usfe}}$$

$D > 1 \Rightarrow \gamma_s > \gamma_{usfe} \Rightarrow$ **Intrinsically Ductile**

$D < 1 \Rightarrow \gamma_s < \gamma_{usfe} \Rightarrow$ **Intrinsically Brittle**

Recent studies have relied on D to assess the intrinsic ductility of refractory alloys [12,63–65]. Fig. 2b shows the D calculated for pure metals and alloys in the form of heat map. The D ranges from 4.16 (TaTi) to 1.81 (MoW). As discussed in Sections 3.2 and 3.3, the ΔE_f influences γ_{usfe} much more strongly than γ_s. Similarly, to understand the relation between ΔE_f and percentage change in D (ΔD, calculated similar to $\Delta\gamma_{usfe}$) from its composition averaged value, we plot ΔD vs. ΔE_f in Fig. 6b. A linear fit to the data in Fig. 6b has a slope of 1.89 with Pearson's r (correlation parameter) of 0.66. The γ_s does not show any specific relationship with E_f as discussed in Section 3.3. However, the γ_{usfe} shows a strong relationship with E_f as discussed in Section 3.2. This indicates a positive influence of ΔE_f on controlling the D of refractory binary alloys. There is a positive correlation between ΔD and ΔE_f, but it is not as strong as that of γ_{usfe}, since it has contribution from γ_s as well.

The WRe and MoRe has the largest positive ΔD as observed from Fig. 6b. Large positive ΔD of Re containing binary alloys is because of large negative $\Delta\gamma_{usfe}$ (Fig. 5a) primarily due to repulsive nature of bonds between Re-W and Re-Mo atoms and positive $\Delta\gamma_s$ (Fig. 6a). A positive ΔD is observed for majority of alloys containing Group-IV (Ti, Zr, Hf) elements. The positive ΔD explains large ductility reported in Al/Nb/Mo-Ta-Ti-Zr-Hf-V alloy, its sub-systems [20,66–69,70] and NbTaTiZrHf [71,72]. This could be due to large negative $\Delta\gamma_{usfe}$, although $\Delta\gamma_s$ is not favoring ΔD to be positive. The ductility of alloys containing Ti, Zr, and Hf is attributed to the low VEC (< 4.5) [20]. However, VEC criteria fails to explain the role of higher valency Re addition in improving ductility of W and Mo [9,10,14]. The present analysis shows that the enthalpy of formation of alloys gives a fairly reliable idea about deformability of refractory alloys apart from dictating their thermodynamic stability; which can be used as a criterion to design new alloy chemistries with desired ductility.

4. Summary and conclusion

Here we used DFT simulations to calculate the ΔE_f, γ_{usfe}, γ_s, and D of concentrated alloys. We found that the first nearest neighbor has the strongest influence on the γ_{usfe}, hence the shearing interface with formula composition has been chosen for calculating the γ_{usfe}. The calculated γ_{usfe} had maximum error of $\pm$ 30 mJ/m^2. The ΔE_f of the equiatomic binary alloys ranges from -0.25 eV/Atom to 0.17 eV/

Atom. The negative ΔE_f indicates attractive nature of the bonding between the constituents and vice-versa. Here we have shown that the positive ΔE_f shall lead to reduced γ_{usfe} (compared to the composition averaged value) due to the repulsive interaction between the alloy constituents.

Our results suggest that the maximum reduction in γ_{usfe} could be achieved for alloys having positive ΔE_f. Therefore, while selecting the alloying elements one should ensure the positive enthalpy of formation is well compensated by the sufficiently large entropy. Our findings provide an explanation for the addition of low valency Ti, Zr, and Hf as well as high valency Re in improving the ductility of refractory metals and alloys. Our findings also explain the failure of empirical rules for increased ductility of refractory BCC alloys where VEC type criterion can be contradictory to experimental observations (e.g. Re addition in W). Taking the effect of enthalpy of formation on the deformability of concentrated alloys is likely to open new directions in the design of refractory alloys for high-temperature applications.

CRediT authorship contribution statement

Sufyan M. Shaikh: Conceptualization, Methodology, Software, Validation, Formal analysis, Investigation, Data curation, Writing – original draft, Visualization. **B.S. Murty:** Resources, Writing – review & editing, Supervision. **Satyesh K. Yadav:** Conceptualization, Methodology, Writing – review & editing, Resources, Project administration.

Data availability

All the data for the study is in the manuscript.

Declaration of Competing Interest

The authors declare the following financial interests/personal relationships which may be considered as potential competing interests: Co-author is a current editor of the Journal of Alloys and Compounds - BS Murty.

Appendix A. Supporting information

Supplementary data associated with this article can be found in the online version at doi:10.1016/j.jallcom.2022.168597.

References

[1] M. Baker, Defining Pathways for Realizing the Revolutionary Potential of High Entropy Alloys: a TMS Accelerator Study, Tech. Rep. (oct 2021). 10.7449/HEApathways.⟨https://www.TMS.org/HEApathways⟩.

[2] J.-W. Yeh, Recent progress in high-entropy alloys, Ann. Chim. Sci. Des. Matér. 31 (6) (2006) 633–648, https://doi.org/10.3166/acsm.31.633-648 ⟨http://acsm.revuesonline.com/article.jsp?articleId=9099⟩.

[3] B.S. Murty, J.W. Yeh, S. Ranganathan, P.P. Bhattacharjee, 13 - Applications and future directions, in: B.S. Murty, J.W. Yeh, S. Ranganathan, P.P. Bhattacharjee (Eds.), High-EntropyAlloy, second ed., Elsevier, 2019, pp. 247–257 10.1016/B978-0-12-816067-1.00013-8 ⟨http://www.sciencedirect.com/science/article/pii/B9780128160671000138⟩.

[4] R. C. Reed, The Superalloys: Fundamentals and Applications (Google eBook), 2006. ⟨http://books.google.com/books?id=SIUGcd4a-EkC&pgis=1⟩.

[5] O.N. Senkov, D.B. Miracle, K.J. Chaput, J.-P. Couzinie, Development and exploration of refractory high entropy alloys-A review, J. Mater. Res. 33 (19) (2018) 3092–3128, https://doi.org/10.1557/jmr.2018.153 ⟨https://www.cambridge.org/core/product/identifier/S088429141800153X/type/journal_article⟩.

[6] S.M. Shaikh, V. Hariharan, S.K. Yadav, B. Murty, CALPHAD and rule-of-mixtures: a comparative study for refractory high entropy alloys, Intermetallics 127 (2020) 106926, https://doi.org/10.1016/j.intermet.2020.106926

[7] D.B. Miracle, High entropy alloys as a bold step forward in alloy development, Nat. Commun. 10 (1) (2019) 1–3, https://doi.org/10.1038/s41467-019-09700-1

[8] B.S. Murty, J.W. Yeh, S. Ranganathan, P.P. Bhattacharjee, High-Entropy Alloy, second ed., Elsevier, 2019, pp. 13–30 10.1016/B978-0-12-816067-1.00002-3 ⟨http://www.sciencedirect.com/science/article/pii/B9780128160671000023⟩.

[9] C.B. Geller, R.W. Smith, J.E. Hack, P. Saxe, E. Wimmer, A computational search for ductilizing additives to Mo, Scr. Mater. 52 (3) (2005) 205–210, https://doi.org/10.1016/j.scriptamat.2004.09.034

[10] C. Ren, Z.Z. Fang, M. Koopman, B. Butler, J. Paramore, S. Middlemas, Methods for improving ductility of tungsten - a review, Int. J. Refract. Met. Hard Mater. 75 (January) (2018) 170–183, https://doi.org/10.1016/j.ijrmhm.2018.04.012

[11] W.D. Klopp, A review of chromium, molybdenum, and tungsten alloys, J. Less Common Met. 42 (3) (1975) 261–278, https://doi.org/10.1016/0022-5088(75)90046-6

[12] C. Yang, L. Qi, Ab initio calculations of ideal strength and lattice instability in W-Ta and W-Re alloys, Phys. Rev. B 97 (1) (2018) 014107, https://doi.org/10.1103/PhysRevB.97.014107

[13] J. Qian, C. Wu, J. Fan, H. Gong, Effect of alloying elements on stacking fault energy and ductility of tungsten, J. Alloy. Compd. 737 (2018) 372–376, https://doi.org/10.1016/j.jallcom.2017.12.042 ⟨http://linkinghub.elsevier.com/retrieve/pii/S0925838817342172⟩.

[14] Y.-H. Li, H.-B. Zhou, L. Liang, N. Gao, H. Deng, F. Gao, G. Lu, G.-H. Lu, Transition from ductilizing to hardening in tungsten: the dependence on rhenium distribution, Acta Mater. 181 (2019) 110–123, https://doi.org/10.1016/j.actamat.2019.09.035 ⟨https://linkinghub.elsevier.com/retrieve/pii/S1359645419306251⟩.

[15] S. Shi, L. Zhu, H. Zhang, Z. Sun, R. Ahuja, Mapping the relationship among composition, stacking fault energy and ductility in Nb alloys: a first-principles study, Acta Mater. 144 (2018) 853–861, https://doi.org/10.1016/j.actamat.2017.11.029

[16] Y.Y. Zhao, Z.F. Lei, Z.P. Lu, J.C. Huang, T.G. Nieh, A simplified model connecting lattice distortion with friction stress of Nb-based equiatomic high-entropy alloys, Mater. Res. Lett. 7 (8) (2019) 340–346, https://doi.org/10.1080/21663831.2019.1610105

[17] Z.D. Han, H.W. Luan, X. Liu, N. Chen, X.Y. Li, Y. Shao, K.F. Yao, Microstructures and mechanical properties of TixNbMoTaW refractory high-entropy alloys, Mater. Sci. Eng. A 712 (2018) 380–385, https://doi.org/10.1016/j.msea.2017.12.004

[18] V.T. Nguyen, M. Qian, Z. Shi, T. Song, L. Huang, J. Zou, Compositional design of strong and ductile (tensile) Ti-Zr-Nb-Ta medium entropy alloys (MEAs) using the atomic mismatch approach, Mater. Sci. Eng. A 742 (November 2018) (2019) 762–772, https://doi.org/10.1016/j.msea.2018.11.054

[19] S. Huang, W. Li, E. Holmström, L. Vitos, Phase-transition assisted mechanical behavior of TiZrHfTax high-entropy alloys, Sci. Rep. 8 (1) (2018) 12576, https://doi.org/10.1038/s41598-018-30892-x ⟨http://www.nature.com/articles/s41598-018-30892-x⟩.

[20] S. Sheikh, S. Shafeie, Q. Hu, J. Ahlström, C. Persson, J. Veselý, J. Zýka, U. Klement, S. Guo, Alloy design for intrinsically ductile refractory high-entropy alloys, J. Appl. Phys. 120 (16) (2016) 164902, https://doi.org/10.1063/1.4966659

[21] W.D. Klopp, F.C. Holden, R.I. Jaffee, Further Studies on Rhenium Alloying Effects in Molybdenum, Tungsten, and Chromium, Tech. Rep. AD0239687 (jul 1960). ⟨https://apps.dtic.mil/sti/citations/AD0239687⟩.

[22] L. Qi, D.C. Chrzan, Tuning ideal tensile strengths and intrinsic ductility of bcc refractory alloys, Phys. Rev. Lett. 112 (11) (2014) 115503, https://doi.org/10.1103/PhysRevLett.112.115503

[23] D. Wei, X. Li, W. Heng, Y. Koizumi, F. He, W.-M. Choi, B.-j. Lee, H.S. Kim, H. Kato, A. Chiba, Novel Co-rich high entropy alloys with superior tensile properties, Mater. Res. Lett. 7 (2) (2018) 82–88, https://doi.org/10.1080/21663831.2018.1553803

[24] Q. Ding, Y. Zhang, X. Chen, X. Fu, D. Chen, S. Chen, L. Gu, F. Wei, H. Bei, Y. Gao, M. Wen, J. Li, Z. Zhang, T. Zhu, R.O. Ritchie, Q. Yu, Tuning element distribution, structure and properties by composition in high-entropy alloys, Nature 574 (7777) (2019) 223–227, https://doi.org/10.1038/s41586-019-1617-1

[25] D. Wei, X. Li, J. Jiang, W. Heng, Y. Koizumi, W.M. Choi, B.J. Lee, H.S. Kim, H. Kato, A. Chiba, Novel Co-rich high performance twinning-induced plasticity (TWIP) and transformation-induced plasticity (TRIP) high-entropy alloys, Scr. Mater. 165 (2019) 39–43, https://doi.org/10.1016/j.scriptamat.2019.02.018

[26] D. Wei, X. Li, S. Schönecker, J. Jiang, W.M. Choi, B.J. Lee, H.S. Kim, A. Chiba, H. Kato, Development of strong and ductile metastable face-centered cubic single-phase high-entropy alloys, Acta Mater. 181 (2019) 318–330, https://doi.org/10.1016/j.actamat.2019.09.050

[27] R. Zhang, S. Zhao, J. Ding, Y. Chong, T. Jia, C. Ophus, M. Asta, R.O. Ritchie, A.M. Minor, Short-range order and its impact on the CrCoNi medium-entropy alloy, Nature 581 (7808) (2020) 283–287, https://doi.org/10.1038/s41586-020-2275-z

[28] R. Lizárraga, X. Li, D. Wei, L. Vitos, X. Li, The effect of Si and Ge on the elastic properties and plastic deformation modes in high- And medium-entropy alloys, Appl. Phys. Lett. 119 (14) (2021), https://doi.org/10.1063/5.0064939

[29] D. Wei, L. Wang, Y. Zhang, W. Gong, T. Tsuru, I. Lobzenko, J. Jiang, S. Harjo, T. Kawasaki, J.W. Bae, W. Lu, Z. Lu, Y. Hayasaka, T. Kiguchi, N.L. Okamoto, T. Ichitsubo, H.S. Kim, T. Furuhara, E. Ma, H. Kato, Metalloid substitution elevates

simultaneously the strength and ductility of face-centered-cubic high-entropy alloys, Acta Mater. 225 (2022) 117571, https://doi.org/10.1016/j.actamat.2021.117571

[30] D. Wei, W. Gong, T. Tsuru, I. Lobzenko, X. Li, S. Harjo, T. Kawasaki, H.-S. Do, J.W. Bae, C. Wagner, G. Laplanche, Y. Koizumi, H. Adachi, K. Aoyagi, A. Chiba, B.-J. Lee, H.S. Kim, H. Kato, Si-addition contributes to overcoming the strength-ductility trade-off in high-entropy alloys, Int. J. Plast. 159 (2022) 103443, https://doi.org/10.1016/j.ijplas.2022.103443

[31] D. Wei, W. Gong, T. Tsuru, T. Kawasaki, S. Harjo, B. Cai, P.K. Liaw, H. Kato, Mechanical behaviors of equiatomic and near-equiatomic face-centered-cubic phase high-entropy alloys probed using in situ neutron diffraction, Int. J. Plast. 158 (2022) 103417, https://doi.org/10.1016/j.ijplas.2022.103417

[32] S. Liu, Y. Wu, H. Wang, J. He, J. Liu, C. Chen, X. Liu, H. Wang, Z. Lu, Stacking fault energy of face-centered-cubic high entropy alloys, Intermetallics 93 (2018) 269–273, https://doi.org/10.1016/j.intermet.2017.10.004 (https://linkinghub.elsevier.com/retrieve/pii/S0966979517307379).

[33] S. Xu, Y. Su, L.T.W. Smith, I.J.J. Beyerlein, Frank-Read source operation in six body-centered cubic refractory metals, J. Mech. Phys. Solids 141 (2020) 104017, https://doi.org/10.1016/j.jmps.2020.104017

[34] M. Beyramali Kivy, M. Asle Zaeem, Generalized stacking fault energies, ductilities, and twinnabilities of CoCrFeNi-based face centered cubic high entropy alloys, Scr. Mater. 139 (2017) 83–86, https://doi.org/10.1016/j.scriptamat.2017.06.014

[35] L.Y. Tian, R. Lizárraga, H. Larsson, E. Holmström, L. Vitos, A first principles study of the stacking fault energies for fcc Co-based binary alloys, Acta Mater. 136 (2017) 215–223, https://doi.org/10.1016/j.actamat.2017.07.010

[36] W. Li, S. Lu, Q.M. Hu, B. Johansson, S.K. Kwon, M. Grehk, J.Y. Johnsson, L. Vitos, Generalized stacking fault energy of γ -Fe, Philos. Mag. 96 (6) (2016) 524–541, https://doi.org/10.1080/14786435.2016.1140912

[37] M. Chandran, S.K. Sondhi, First-principle calculation of stacking fault energies in Ni and Ni-Co alloy, J. Appl. Phys. 109 (10) (2011), https://doi.org/10.1063/1.3585786

[38] A.J. Zaddach, C. Niu, C.C. Koch, D.L. Irving, Mechanical properties and stacking fault energies of NiFeCrCoMn high-entropy alloy, JOM 65 (12) (2013) 1780–1789, https://doi.org/10.1007/s11837-013-0771-4

[39] S. Zhao, Y. Osetsky, G.M. Stocks, Y. Zhang, Local-environment dependence of stacking fault energies in concentrated solid-solution alloys, npj Comput. Mater. 5 (1) (2019) 13, https://doi.org/10.1038/s41524-019-0150-y

[40] A. van de Walle, M. Asta, G. Ceder, The alloy theoretic automated toolkit: a user guide (arXiv:0212159). Calphad 26 (4) (2002) 539–553, https://doi.org/10.1016/S0364-5916(02)80006-2

[41] A. Van De Walle, P. Tiwary, M. De Jong, D.L. Olmsted, M. Asta, A. Dick, D. Shin, Y. Wang, L.Q. Chen, Z.K. Liu, Efficient stochastic generation of special quasirandom structures, Calphad Comput. Coupling Phase Diagr. Thermochem 42 (2013) 13–18, https://doi.org/10.1016/j.calphad.2013.06.006

[42] Y. Xu, M. Yamazaki, P. Villars, Inorganic materials database for exploring the nature of material, Jpn. J. Appl. Phys. 50 (11 PART 2) (2011), https://doi.org/10.1143/JJAP.50.11RH02

[43] K. Momma, F. Izumi, VESTA 3 for three-dimensional visualization of crystal, volumetric and morphology data, J. Appl. Crystallogr. 44 (6) (2011) 1272–1276, https://doi.org/10.1107/S0021889811038970

[44] G. Kresse, J. Hafner, Ab initio molecular dynamics for liquid metals, Phys. Rev. B 47 (1) (1993) 558–561, https://doi.org/10.1103/PhysRevB.47.558

[45] P.E. Blöchl, Projector augmented-wave method, Phys. Rev. B 50 (24) (1994) 17953–17979, https://doi.org/10.1103/PhysRevB.50.17953

[46] G. Kresse, J. Furthmüller, Efficient iterative schemes for ab initio total-energy calculations using a plane-wave basis set, Phys. Rev. B 54 (16) (1996) 11169–11186, https://doi.org/10.1103/PhysRevB.54.11169

[47] J.P. Perdew, K. Burke, M. Ernzerhof, Generalized gradient approximation made simple, Phys. Rev. Lett. 77 (18) (1996) 3865–3868, https://doi.org/10.1103/PhysRevLett.77.3865

[48] D. Joubert, From ultrasoft pseudopotentials to the projector augmented-wave method, Phys. Rev. B Condens. Matter Mater. 59 (3) (1999) 1758–1775, https://doi.org/10.1103/PhysRevB.59.1758

[49] M. Methfessel, A.T. Paxton, High-precision sampling for Brillouin-zone integration in metals, Phys. Rev. B 40 (6) (1989) 3616–3621, https://doi.org/10.1103/PhysRevB.40.3616

[50] H.J. Monkhorst, J.D. Pack, Special points for Brillouin-zone integrations, Phys. Rev. B 13 (12) (1976) 5188–5192, https://doi.org/10.1103/PhysRevB.13.5188

[51] A. Van de Walle, G. Ceder, The effect of lattice vibrations on substitutional alloy thermodynamics (arXiv:0106490). Rev. Mod. Phys. 74 (1) (2002) 11–45, https://doi.org/10.1103/RevModPhys.74.11

[52] D. Shin, A. van de Walle, Y. Wang, Z.-K. Liu, First-principles study of ternary fcc solution phases from special quasirandom structures (arXiv:0709.2302). Phys. Rev. B 76 (14) (2007) 144204, https://doi.org/10.1103/PhysRevB.76.144204

[53] Re-V Binary Phase Diagram 0–100 at% V: Datasheet from "PAULING FILE Multinaries Edition - 2012" in SpringerMaterials (2012). (https://materials.springer.com/isp/phase-diagram/docs/c_0902814).

[54] Re-Ta Binary Phase Diagram 0–100 at% Ta: Datasheet from "PAULING FILE Multinaries Edition - 2012" in SpringerMaterials (2012). (https://materials.springer.com/isp/phase-diagram/docs/c_0100260).

[55] Hf-W Binary Phase Diagram 0–100 at% W: Datasheet from "PAULING FILE Multinaries Edition - 2012" in SpringerMaterials (2012). (https://materials.springer.com/isp/phase-diagram/docs/c_0907545).

[56] W-Zr Binary Phase Diagram 0–100 at% Zr: Datasheet from "PAULING FILE Multinaries Edition - 2012" in SpringerMaterials (2012). (https://materials.springer.com/isp/phase-diagram/docs/c_0904967).

[57] Hf-V Binary Phase Diagram 0–100 at% V: Datasheet from "PAULING FILE Multinaries Edition - 2012" in SpringerMaterials (2012). (https://materials.springer.com/isp/phase-diagram/docs/c_0100184).

[58] V-Zr Binary Phase Diagram 0–100 at% Zr: Datasheet from "PAULING FILE Multinaries Edition - 2012" in SpringerMaterials (2012). (https://materials.springer.com/isp/phase-diagram/docs/c_0905433).

[59] Re-W Binary Phase Diagram 0–100 at% W: Datasheet from "PAULING FILE Multinaries Edition - 2012" in SpringerMaterials (2012). (https://materials.springer.com/isp/phase-diagram/docs/c_0904355).

[60] A. Zunger, S.-H. Wei, L.G. Ferreira, J.E. Bernard, Special quasirandom structures, Phys. Rev. Lett. 65 (3) (1990) 353–356, https://doi.org/10.1103/PhysRevLett.65.353

[61] U.V. Waghmare, E. Kaxiras, V.V. Bulatov, M.S. Duesbery, Effects of alloying on the ductility of MoSi 2 single crystals from first-principles calculations, Model. Simul. Mater. Sci. Eng. 6 (4) (1998) 493–506, https://doi.org/10.1088/0965-0393/6/4/013

[62] J.R. Rice, Dislocation nucleation from a crack tip: an analysis based on the Peierls concept, J. Mech. Phys. Solids 40 (2) (1992) 239–271, https://doi.org/10.1016/S0022-5096(05)80012-2 (https://linkinghub.elsevier.com/retrieve/pii/S0022509605800122).

[63] Y.-J. Hu, A. Sundar, S. Ogata, L. Qi, Screening of generalized stacking fault energies, surface energies and intrinsic ductile potency of refractory multi-component alloys (arXiv:2008.03591). Acta Mater. 210 (2021) 116800, https://doi.org/10.1016/j.actamat.2021.116800 arXiv:2008.03591 (https://linkinghub.elsevier.com/retrieve/pii/S1359645421001804).

[64] O.N. Senkov, D.B. Miracle, Generalization of intrinsic ductile-to-brittle criteria by Pugh and Pettifor for materials with a cubic crystal structure, Sci. Rep. 11 (1) (2021) 10–13, https://doi.org/10.1038/s41598-021-83953-z

[65] E. Mak, B. Yin, W.A. Curtin, A ductility criterion for bcc high entropy alloys, J. Mech. Phys. Solids 152 (July 2020) (2021) 104389, https://doi.org/10.1016/j.jmps.2021.104389

[66] B. Schuh, B. Völker, J. Todt, N. Schell, L. Perrière, J. Li, J.P. Couzinié, A. Hohenwarter, Thermodynamic instability of a nanocrystalline, single-phase TiZrNbHfTa alloy and its impact on the mechanical properties, Acta Mater. 142 (2018) 201–212, https://doi.org/10.1016/j.actamat.2017.09.035

[67] C.C. Juan, M.H. Tsai, C.W. Tsai, W.L. Hsu, C.M. Lin, S.K. Chen, S.J. Lin, J.W. Yeh, Simultaneously increasing the strength and ductility of a refractory high-entropy alloy via grain refining, Mater. Lett. 184 (2016) 200–203, https://doi.org/10.1016/j.matlet.2016.08.060

[68] S.Y. Chen, L. Wang, W.D. Li, Y. Tong, K.K. Tseng, C.W. Tsai, J.W. Yeh, Y. Ren, W. Guo, J.D. Poplawsky, P.K. Liaw, Peierls barrier characteristic and anomalous strain hardening provoked by dynamic-strain-aging strengthening in a body-centered-cubic high-entropy alloy, Mater. Res. Lett. 7 (12) (2019) 475–481, https://doi.org/10.1080/21663831.2019.1658233

[69] L. Casillas-Trujillo, U. Jansson, M. Sahlberg, G. Ek, M.M. Nygård, M.H. Sørby, B.C. Hauback, I.A. Abrikosov, B. Alling, Interstitial carbon in bcc HfNbTiVZr high-entropy alloy from first principles, Phys. Rev. Mater. 4 (12) (2020) 123601, https://doi.org/10.1103/PhysRevMaterials.4.123601

[70] V. Soni, O.N. Senkov, B. Gwalani, D.B. Miracle, R. Banerjee, Microstructural Design for Improving Ductility of An Initially Brittle Refractory High Entropy Alloy, Sci. Rep. 8 (1) (2018) 1–10, https://doi.org/10.1038/s41598-018-27144-3

[71] O. Senkov, J. Scott, S. Senkova, D. Miracle, C. Woodward, Microstructure and room temperature properties of a high-entropy TaNbHfZrTi alloy, J. Alloy. Compd. 509 (20) (2011) 6043–6048, https://doi.org/10.1016/j.jallcom.2011.02.171 (https://linkinghub.elsevier.com/retrieve/pii/S0925838811005536).

[72] O.N. Senkov, S.L. Semiatin, Microstructure and properties of a refractory high-entropy alloy after cold working, J. Alloy. Compd. 649 (2015) 1110–1123, https://doi.org/10.1016/j.jallcom.2015.07.209 (https://www.sciencedirect.com/science/article/pii/S0925838815306071).